Estimation, Smoothing, and Characterization of Apparent Diffusion Coefficient Profiles from High Angular Resolution DWI

Y.Chen[1], W.Guo[1], Q.Zeng[1], X.Yan[1], F.Huang[1], H.Zhang[1],
G. He[2], B.C.Vemuri[3], Y.Liu[2]
University of Florida, [1]Dept. of Mathematics, [2]Dept. of Psychiatry and Neuroscience
[3]Dept. of Computer and Information Science and Engineering

Abstract

We present a new variational framework for recovery of apparent diffusion coefficient (ADC) from High Angular Resolution Diffusion-weighted (HARD) MRI. The model approximates the ADC profiles by a 4th order spherical harmonic series (SHS), whose coefficients are obtained by solving a constrained minimization problem. By minimizing the energy functional, the ADC profiles are estimated and regularized simultaneously across the entire volume. In this model, feature preserving smoothing is achieved by minimizing a non-standard growth functional, and the estimation is based on the original Stejskal-Tanner equation. The antipodal symmetry and positiveness of the ADC are also accommodated into the model. Furthermore, coefficients of the SHS and the variance of ADC profiles from its mean are used to characterize the diffusion anisotropy. The effectiveness of the proposed model is depicted via application to both simulated and HARD MRI human brain data. The characterization of non-Gaussian diffusion based on the proposed model showed consistency with known neuroanatomy.

1 Introduction

Diffusion-weighted MRI (DW-MRI, shorten as DWI) adds to conventional MRI the capability of measuring the random motion of water molecules, referred to as diffusion. The diffusion of water molecules in tissues over a time interval t can be described by a probability density function p_t on the displacement $\mathbf{r}$. Since $p_t(\mathbf{r})$ is largest in the directions of least hindrance to diffusion and smaller in other directions, the information about $p_t(\mathbf{r})$ reveals fiber orientations and leads to meaningful inferences about the microstructure of tissues. This characteristic of the diffusion is termed as anisotropy. Changes in these tissue properties can often be correlated with processes that occur in development, degeneration, disease, and aging, so this method has become more and more widely applied ([1, 2, 3, 4]).

The density function p_t is related to DWI echo signal $s(\mathbf{q})$ via a Fourier transformation (FT) with respect to $\mathbf{q}$, which represents the direction of the diffusion sensitizing gradients, by

$$s(\mathbf{q}) = s_0 \int p_t(\mathbf{r}) e^{i\mathbf{q}\cdot\mathbf{r}} d\mathbf{r}, \tag{1.1}$$

where s_0 is the MRI signal in the absence of any gradient. Therefore, $p_t(\mathbf{r})$ can be estimated from the inverse FT of $s(\mathbf{q})/s_0$. Recently, Tuch et al. ([5]) introduced the method of HARD MRI, and Wedeen et al. ([6]) succeed in acquiring 500 measurements of $s(\mathbf{q})$ in each scan to perform a fast FT inversion. However, this method requires a large number of measurements of $s(\mathbf{q})$ over a wide range of $\mathbf{q}$ in order to perform a stable inverse FT.

One of the alternative for identifying voxels containing crossing fibers is using ADC profiles $d(\mathbf{x}, \theta, \phi)$, which can be related to the observed signal in DWI through the Stejskal-tanner equation:

$$s(\mathbf{x}, \mathbf{q}) = s_0(\mathbf{x}) e^{-bd(\mathbf{x},\theta,\phi)}, \tag{1.2}$$

where (θ, ϕ) $(0 \le \theta < \pi,\ 0 \le \phi < 2\pi)$ represents the direction of $\mathbf{q}$, and $b = \gamma^2\delta^2|q|^2(\Delta - \delta/3)$. Here γ is the gyromagnetic ratio, and δ is the duration of two magnetic field gradient pulses with a separation time Δ in the use of Stejskal-tanner pulsed gradient spin echo method ([7]). For Gaussian diffusion, where p_t is assumed to be a Gaussian, $d(\mathbf{u}) = b\mathbf{u}^T D\mathbf{u}$. The trace, eigenvalues and eigenfunctions of D has been used to characterize the anisotropy and directional properties of the diffusion. This is known as diffusion tensor imaging (DTI), and in particular useful for creating white matter fiber tracts ([8, 9, 10, 11, 12, 13]).

However, it has been recognized that the Gaussian diffusion model is inappropriate for assessing multiple fiber tract orientations, when complex tissue structure is found within a voxel ([9, 14, 15, 16, 5, 6]). For non-Gaussion diffusion Frank ([16]), also Alexander et al. ([17]) used SHS approximation of the ADC profiles estimated from HARD data to characterize the diffusion anisotropy. In the work of [16, 17] $d(\mathbf{x}, \theta, \phi)$ was computed from HARD raw data via the linearized form of (1.2):

$$d(\mathbf{q}) = -\frac{1}{b} log \frac{s(\mathbf{q})}{s_0}. \tag{1.3}$$

Proceedings of the 2004 IEEE Computer Society Conference on Computer Vision and Pattern Recognition (CVPR'04)
1063-6919/04 $20.00 © 2004 **IEEE**

and represented by a truncated SHS:

$$d(\mathbf{x},\theta,\phi)=\sum_{l=0}^{l_{max}}\sum_{m=-l}^{l}A_{l,m}(\mathbf{x})Y_{l,m}(\theta,\phi), \qquad (1.4)$$

where $Y_{l,m}(\theta,\phi)$ are the spherical harmonics, which are complex valued functions defined on S^2. The odd-order terms in the SHS are set to be zero, since the HARD measurements are made by a series of 3-d rotation, $d(\theta,\phi)$ is real and antipodal symmetry. The coefficients $A_{l,m}(\mathbf{x})$ for even l are determined by

$$A_{l,m}(\mathbf{x})=\int_0^{2\pi}\int_0^{\pi}-\frac{1}{b}log\frac{s(\mathbf{q})}{s_0}Y^*_{l,m}(\theta,\phi)sin\theta d\theta d\phi \qquad (1.5)$$

in [16], where $*$ denotes the complex conjugate, and as the least-squares solutions of

$$-\frac{1}{b}log\frac{s(\mathbf{x},\theta,\phi)}{s_0(\mathbf{x})}=\sum_{l=0}^{l_{max}}\sum_{m=-l}^{l}A_{l,m}(\mathbf{x})Y_{l,m}(\theta,\phi) \qquad (1.6)$$

in [17]. Furthermore, they used these $A_{l,m}(\mathbf{x})$'s to charaterize the diffusion anisotropy. The voxels with the significant 4th order ($l=4$) components in SHS are characterized as anisotropic with two-fiber orientations (henceforth simply called two-fiber), while voxels with the significant 2nd order ($l=2$) but not the 4th order components are classified as anisotropic with single fiber orientation (called the one-fiber), which is equivalent to the DTI model. Voxels with the significant 0th order ($l=0$) but not the 2nd and 4th order components are classified as isotropic. The truncated order becomes higher as the structure complexity increases. Their experimental results showed that non-Gaussian profiles arise consistently in various brain regions where complex tissue structure is known to exist.

Since the ADC profiles can be used to characterize the diffusion anisotropy, it is of great significance to have an accurate estimate of it. In general the raw HARD MRI data are noisy. Computing the coefficients of SHS directly from the raw data often provides poor estimates. As a result, it will lead to inaccurate or false characterization of the diffusion and consequently leads to incorrect fiber tracking. Therefore, designing models that can perform denoising with relevant features preserved in the process of estimating the ADC profiles from noisy raw HARD data is important.

However, very few methods reported in literature to date on HARD data analysis have considered the denoising problem in the reconstruction of the ADC profiles. While the HARD raw data is noisy. To improve the accuracy of the estimation, in this paper we present a novel model that has the ability of simultaneously smoothing and estimating the ADC profile $d(\mathbf{x},\theta,\phi)$ from the noisy HARD measurements $s(\mathbf{x},\mathbf{q})$ while preserving the relevant features, and the positiveness and antipodal symmetry constraints of $d(\mathbf{x},\theta,\phi)$. Our approach differs from the existing approaches developed in [16] and [17] mainly in the aspect of recovering $A_{l,m}(\mathbf{x})$. In our approach the $A_{l,m}(\mathbf{x})$'s are reconstructed over the entire volume through a joint estimation and regularization rather than estimating them individually at each isolated voxel. Moreover, in this paper we provide a method for characterizing the diffusion anisotropy, which uses not only the information of $A_{l,m}(\mathbf{x})$'s as in [16, 17], but also the variation of $d(\theta,\phi)$ about its mean. Our experimental results showed the effectiveness of the model in the estimation and enhancement of anisotropy of the ADC profile. The characterization of the diffusion anisotropy based on the reconstructed ADC profiles using the proposed model is consistent with the known fiber anatomy.

2 Proposed model

In this paper we consider the cases where the maximum number of fibers within a single voxel is two. Employing the idea developed in [16, 17], we approximate d by (1.6) with $l_{max}=4$. Note that $d(\theta,\phi)$ is a real valued function, and $Y_{l,m}$ satisfies $Y_{l,-m}=(-1)^mY^*_{l,m}$, $A_{l,m}$ is constrained by $A_{l,-m}=(-1)^mA^*_{l,m}$. This constraint reduces the 15 unknown complex-valued coefficients $A_{l,m}$ in (1.6) to 15 real valued functions. They are

$$A_{l,0}(\mathbf{x}),\ ReA_{l,m}(\mathbf{x}),\ ImA_{l,m}(\mathbf{x}),(l=0,2,4,\ \ m=1\ldots l). \qquad (2.1)$$

By using (2.1), we can rewrite (1.6) as

$$d(\mathbf{x},\theta,\phi)=\sum_{l=0,2,4}A_{l,0}(\mathbf{x})Y_{l,0}(\theta,\phi)+2\sum_{l=2,4}\sum_{m=1}^{l}$$

$$(ReA_{l,m}(\mathbf{x})ReY_{l,m}(\theta,\phi)-ImA_{l,m}(\mathbf{x})ImY_{l,m}(\theta,\phi)) \qquad (2.2)$$

where ReF and ImF represent the real and imaginary part of a function F respectively. To get a regularized estimation for the functions in (2.1), we solve the following constrained minimization problem:

$$\min\frac{1}{2}\int_\Omega\{(\int_0^{2\pi}\int_0^{\pi}|s(\mathbf{x},\theta,\phi)-\tilde{s}_0(\mathbf{x})e^{-bd(\mathbf{x},\theta,\phi)}|^2sin\theta d\theta d\phi)$$

$$+\alpha|\tilde{s}_0(\mathbf{x})-s_0(\mathbf{x})|^2\}d\mathbf{x}+\lambda\int_\Omega\{\sum_{l=0,2,4}|\nabla A_{l,0}|^{p(\mathbf{x})}$$

$$+\sum_{l=2,4}\sum_{m=-l}^{l}(|\nabla ReA_{l,m}(\mathbf{x})|^{p(\mathbf{x})}+|\nabla ImA_{l,m}(\mathbf{x})|^{p(\mathbf{x})})$$

$$+|\nabla\tilde{s}_0(\mathbf{x})|^{q(\mathbf{x})}\}d\mathbf{x}, \qquad (2.3)$$

with the constraint:

$$d(\mathbf{x}, \theta, \phi) > 0. \tag{2.4}$$

The minimization is taken with respect to $A_{l,0}(\mathbf{x})$, $ReA_{l,m}(\mathbf{x})$, $ImA_{l,m}(\mathbf{x})$, and $\tilde{s}_0(\mathbf{x})$. In (2.3)-(2.4) d is represented by (2.2), $\lambda > 0$ is a parameter, and

$$p(\mathbf{x}) = 1 + \frac{1}{1 + k|\nabla G_\sigma * A_{l,m}|^2},$$

$$q(\mathbf{x}) = 1 + \frac{1}{1 + k|\nabla G_\sigma * s_0|^2}. \tag{2.5}$$

with parameters $k,\ \sigma > 0$, and the Gaussian kernel G_σ. The first two terms in (2.3) are the data fidelity term. The data constraint for $A_{l,m}(\mathbf{x})$ is based on the original Stejskal-tanner equation (1.2) rather than its (log) linearized form (1.3). As observed in [18] when the signal to noise ratio is low the linearized model gives different results from the original nonlinear Stejskal-Tanner model in the tensor field estimation from DTI. The last four terms in (2.3) are the regularization terms for $A_{l,m}(\mathbf{x})$ and $\tilde{s}_0(\mathbf{x})$. The speed and the direction of diffusion governed by these terms at each point $\mathbf{x}$ vary according to the magnitude of its gradient. By the choice of $p(\mathbf{x})$ (correspondingly for $q(\mathbf{x})$)

$$\lim_{|\nabla A_{l,m}(\mathbf{x})| \to 0} p(\mathbf{x}) = 2, \quad and \quad \lim_{|\nabla A_{lm}(\mathbf{x})|(\mathbf{x}) \to \infty} p(\mathbf{x}) = 1.$$

Then, at the locations where the magnitudes of these image gradients are high, $p(\mathbf{x}) \approx 1$, the diffusion by this model is based on minimizing the total variation norm ([19, 20, 21]). The direction of the diffusion is strictly tangential to the edges. In homogeneous regions the image gradients are very small, $p(\mathbf{x}) \approx 2$, and the diffusion is essentially isotropic. At all other locations, the image gradient forces $1 < p < 2$, and the diffusion is between isotropic and total variation based schemes and varies depending on the local properties of the image. Therefore, the smoothing resulting from this model preserves the features in $A_{l,m}(\mathbf{x})$'s, and $s_0(\mathbf{x})$. The constraint (2.4) preserves the positiveness of d.

3 Characterization of anisotropy

In [16] Frank used the $|A_{lm}(\mathbf{x})|$ in the truncated SHS (2.1) to characterize the diffusion anisotropy at each voxel $\mathbf{x}$. Our experimental results, however, indicate that using the information of $|A_{l,m}|$ is insufficient to separate isotropic diffusion, one-fiber diffusion, and multi-fibers diffusion within a voxel. We propose to combine the information from $|A_{l,m}|$ with the variances of $d(\phi, \theta)$ about its mean value to characterize the diffusion anisotropy. We outlined our algorithm as follows:

1. If

$$R_0 =: |A_{0,0}| / \sum_{l=0,2,4} \sum_{m=-l}^{l} |A_{l,m}|, \tag{3.1}$$

is large, or the variance of $d(\theta, \phi)$ about its mean is small, the diffusion at such voxels is classified as isotropic.

2. For the remaining voxels, if

$$R_2 =: \sum_{m=-2}^{m=2} |A_{2,m}| / \sum_{l=0,2,4} \sum_{m=-l}^{l} |A_{l,m}|, \tag{3.2}$$

is large, the diffusion at such voxels is characterized as one-fiber diffusion.

3. For each uncharacterized voxel after the above two steps, search the directions (θ, ϕ), where $d(\theta, \phi)$ attains its local maximums. If there is only one local maximum, d is viewed as one-fiber diffusion. For the rest of the voxels that have more than one local maximum (say 3), the diffusion anisotropy is further characterized by the weights:

$$W_i =: \frac{d(\theta_i, \phi_i) - d_{min}}{\sum_{i=1}^{3} d(\theta_i, \phi_i) - 3d_{min}},$$

where (θ_i, ϕ_i) $(i = 1, 2, 3)$ are the directions in which d attains 3 local maxima. If one of the weights is significant, it is considered as one fiber diffusion. If two weights are similar but much larger than the third one, it is viewed as two-fiber diffusion, if all three weights are similar, it is classified as isotropic diffusion, since we are only interested in discriminating between isotropic, one-fiber or two-fiber diffusions.

4 Experimental results

In this section, we present synthetic as well as real data experiments.

1. Analysis of simulated data

The aim of our experiment on the simulated data is to test whether our model can efficiently reconstruct a regularized ADC profile from the noisy HARD measurements. We simulated an ADC profile on a 3d lattice of dimension $6 \times 6 \times 5$. The volume consists of two homogeneous regions. One of them was generated by taking $s_0(\mathbf{x}) = 562$, $A_{0,0} = 6.28 \times 10^{-3}$, $A_{2,0} = -8.81 \times 10^{-4}$, $A_{4,0} = 6.15 \times 10^{-5}$, $ReA_{2,1} = 5.22 \times 10^{-3}$, $ReA_{2,2} = 5.08 \times 10^{-4}$, $ReA_{4,1} = -8.47 \times 10^{-5}$, $ReA_{4,2} = 4.92 \times 10^{-5}$, $ReA_{4.3} = 3.10 \times 10^{-5}$, $ReA_{4.4} = -1.38 \times 10^{-4}$, $ImA_{2,1} = -1.82 \times 10^{-4}$, $ImA_{2,2} = -1.13 \times 10^{-3}$, $ImA_{4,1} = 9.62 \times 10^{-5}$, $ImA_{4,2} = 3.46 \times 10^{-5}$, $ImA_{4.3} = -3.58 \times 10^{-6}$, $ImA_{4.4} = 1.75 \times 10^{-5}$. The other part was corresponding to $s_0(\mathbf{x}) = 378$, $A_{0,0} = 6.08 \times 10^{-3}$, $A_{2,0} = 2.04 \times 10^{-4}$, $A_{4,0} = 2.63 \times 10^{-4}$, $ReA_{2,1} = 6.63 \times 10^{-5}$, $ReA_{2,2} = -9.71 \times 10^{-5}$, $ReA_{4,1} = 1.27 \times 10^{-4}$,

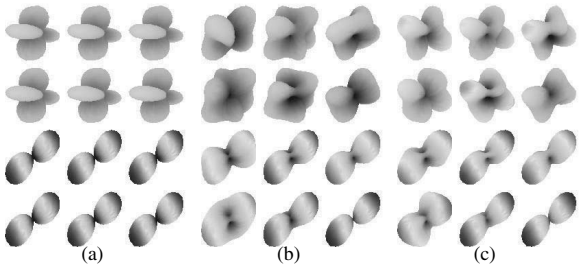

Figure 1: (a) True d, (b) The d generated by (2.2), where the $A_{l,m}$'s are the least-squares solution of (1.6) with the noisy measurement s, (c) Recovered d by applying model (2.3).

$ReA_{4,2} = 2.22 \times 10^{-4}$, $ReA_{4.3} = 1.24 \times 10^{-4}$, $ReA_{4.4} = 4.19 \times 10^{-5}$, $ImA_{2,1} = 5.77 \times 10^{-6}$, $ImA_{2,2} = 9.56 \times 10^{-6}$, $ImA_{4,1} = 6.51 \times 10^{-5}$, $ImA_{4,2} = 6.64 \times 10^{-5}$, $ImA_{4.3} = 7.52 \times 10^{-5}$, $ImA_{4.4} = 3.71 \times 10^{-5}$. In Fig.1a-1c we displayed the true, noisy, and recovered ADC profiles , respectively for a particular slice of size 4 extracted from the volume $6 \times 6 \times 5$. The ADC profile $d(\mathbf{x}, \theta, \phi)$ was computed by (2.2) based on these simulated data, and the corresponding $s_{true}(\mathbf{x}, \theta, \phi)$ was constructed via (1.2) with $b = 1000 s/mm^2$. Then the noisy HARD MRI signal s was generated by adding a zero mean Gaussian noise with standard deviation $\sigma = 0.5$. We then applied our model (2.3) to the noisy $s(\mathbf{x}, \theta, \phi)$ to obtain 15 reconstructed functions in (2.1), and then to get $d(\mathbf{x}, \theta, \phi)$ via (2.2). The reconstructed $d(\mathbf{x}, \theta, \phi)$ is shown in Fig. 1c. The ADC profiles d in Fig.1b were computed by (2.2), where $A_{l,m}$'s are the least-squares solutions of (1.6) with the noisy s. Comparing Figures 1a-1c, it is clear that the noisy measurements s have changed Fig.1a, the original shapes of d, into Fig. 1b. After applying our model (2.3) to reconstruct the ADC profiles, the shapes of d in Fig. 1a were recovered, as shown in Fig. 1c. These simulated results demonstrate that our model is effective in recovering ADC profiles.

2. Analysis of human MRI data

The aim of the second test is to reconstruct and characterize ADC profiles $d(\mathbf{x}, \theta, \phi)$ from human HARD MRI.

The raw DWI data, which usually contains a certain level of noise, were obtained on a GE 3.0 Tesla scanner using a single shot spin-echo EPI sequence. The scanning parameters for the DWI acquisition are: repetition time (TR)=1000ms, echo time (TE) =85ms, the field of view (FOV)=220 mm x 220 mm. 24 axial sections covering the entire brain with the slice thickness=3.8 mm and the intersection gap=1.2 mm. The diffusion-sensitizing gradient encoding is applied in fifty-five directions (selected for the HARD MRI acquisition) with $b = 1000 s/mm^2$. Thus, a total of fifty-six diffusion-weighted images, with a matrix size of 256 x 256, were obtained for each slice section. We applied model (2.3) to these data to obtain all the coefficients $A_{l,m}$'s in (2.1), and determined $d(\mathbf{x}, \theta, \phi)$ using (2.2).

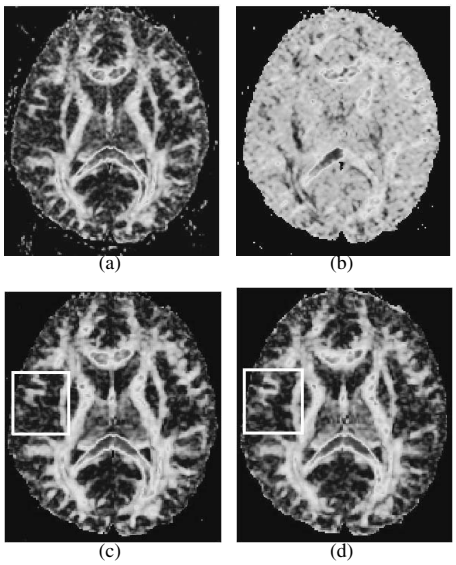

Figure 2: (a) FA from GE software, (b)-(d) R_2 with the $A_{l,m}$'s as the solutions of (1.5), least-squares solutions of (1.6), and model solutions, respectively.

These $A_{l,m}(\mathbf{x})$s are then used to calculate R_0 and R_2 defined in (3.1) and (3.2), respectively, as well as the variance $\sigma(\mathbf{x})$ of $d(\mathbf{x}, \theta, \phi)$ about its mean: $\sigma(\mathbf{x}) = \int_0^{\pi} \int_0^{2\pi} (d(\mathbf{x}, \theta, \phi) - \sum_{i=1}^{55} d(\mathbf{x}, \theta_i, \phi_i)/55)^2 d\theta d\phi$. Based on results from the HARD MRI data of this particular subject, we characterized the diffusion anisotropy according to the following procedure. If $R_0(\mathbf{x}) > 0.856$, or $\sigma(\mathbf{x}) < 19.65$ the diffusion at $\mathbf{x}$ is classified as isotropic. For the remaining voxels if $R_2(\mathbf{x}) > 0.75$, the diffusion at such voxels is considered as one-fiber diffusion. For uncharaterized voxels from these two steps we further classified them by the principles stated in the section 3. The thresholds mentioned above for R_0, R_2 and σ were selected by using their histograms.

Fig. 2 shows the FA and R_2 maps obtained from different models. Fig. 2a displays the FA map from DTI model obtained by using advanced system software from GE. The $A_{l,m}(\mathbf{x})$'s used to obtain $R_2(\mathbf{x})$ in Fig. 2b are directly computed from (1.5). Those used to obtain $R_2(\mathbf{x})$ in Figs. 2c and 2d are the least-squares solutions of (1.6) and the solutions of (2.3), respectively.

Although the image in Fig. 2a is obtained from a conventional DTI model, nevertheless it is comparable with the R_2 map, since single tensor diffusion characterized by SHS representation from the HARD images agrees with that characterized by the DTI model. However, in DTI, a voxel

with a low FA indicates isotropic diffusion, while in our model, multi-fibers diffusion may occur at the location with a low R_2.

From Figs. 2a-2d, it is obvious that characterization of anisotropic diffusion is enhanced. Fig. 2b indicates that the estimations of $A_{l,m}$ directly from the log signals using the least-squares solution of (1.6) are usually nonsmooth. This is evident from a comparison of the anatomic regions inside the white square in Figs. 2c and 2d (zoomed versions of Figs. 3a and 3b, respec.) There is a dark broken line depicted on the map of the external capsule (arrow to the right on Fig. 3a), this same region was recovered by the proposed model and characterized by the third step in our algorithm as the two-fiber anisotropic diffusion (arrow to the right in Fig. 3b) case. Our results also show the connection in a cortical associative tract (arrow to the left in Figs. 3b), however, this connection was not mapped out in Fig. 2c (or Fig. 3a). All these mapped connections are consistent with the known neuroanatomy.

Fig. 4a shows a partition of isotropic, one-fiber, and two-fiber diffusion for the same slice used in getting the figures 2-3. The two-fiber, one-fiber, and isotropic diffusion regions were further characterized by the white, gray, and black regions respectively. The region inside the white box in Fig. 4a, which is the same one indicated within the box in Figs. 2c and 2d, is shown in a zoomed in view in Fig. 3c. Observe that the two arrows in figure 3C are pointing to voxels that have been classified (white color) as locations corresponding to 2-fiber diffusion cases. The characterization of the anisotropy at these voxels and their neighborhoods is consistent with the known neuroanatomy.

Fig. 4b represents the shapes of $d(\mathbf{x}, \theta, \phi)$ at three particular voxels (upper, middle and lower rows). The d in all three voxels is computed using (2.2). However, the $A_{l,m}(\mathbf{x})$ used in computing d depicted in the left column are the least-squares solutions of (1.6), while those in the right column are the solutions obtained from the proposed model (2.3). The profiles corresponding to ds obtained using the least-squares approach as depicted in the first column may be wrongly interpreted as those caused by isotropic diffusion. However, the corresponding profiles using our method correctly depict the expected shapes corresponding to two and one fiber diffusion cases.

5 Conclusions

A novel variational framework was introduced for simultaneous smoothing and estimation of ADC profiles in the form of truncated SHS based on HARD MRI. To our knowledge this is the first attempt to simultaneously reconstruct and regularize the field of ADC profiles from human HARD MRI data. This model is characterized by minimizing a nonstandard growth function with nonlinear data fitting.

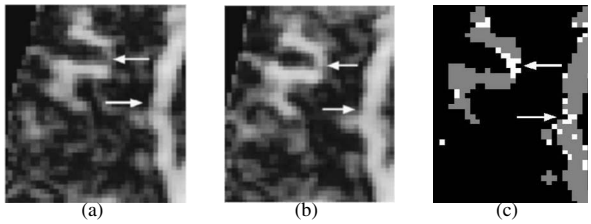

Figure 3: (a)-(b) Enlarged portions inside the white squares in Figs. 2c and 2d, respectively. (c) Enlarged portions inside the white squares in Fig. 4a.

Moreover, the constraints on the positiveness and antipodal symmetry properties of d is also accommodated in this model.

Our experiments on both synthetic and human HARD MRI data showed the effectiveness of the proposed model in the estimation of ADC profiles and the enhancement of the characterization of diffusion anisotropy. The characterization of non-Gaussian diffusion from the proposed method is consistent with the known neuroanatomy.

The choice of parameters in the variational formulation (equation 2.3), however, may affect the results. Our choice is made based on the principle that classification for one-fiber diffusion from the model solution should agree with a priori knowledge of the fiber connections. In this article, we have not included the work for determination of fiber directions and the method for automated fiber tracking. The study addressing these problems will be the focus of our future research efforts.

References

[1] D.LeBihan and P.J.Basser, "Molecular diffusion and nuclear magnetic resonance," *Diffusion and perfusion magnetic resonance imaging*, 1995.

[2] M.E.Moseley, Y.Cohen, J.Mintorovitch, J.suruda L.Chileuitt, D.Norman, and P.Weinstein, "Evidence of anisotropic self-diffusion in cat brain," in *Proc. of the 8th ISMRM*, Amsterdam, 1989, p. 136.

[3] M.E. Moseley, J. Kucharczyk, H.S. Asgari, and D. Norman, "Anisotropy in diffusion weighted mri," *Magn. Reson. Med.*, vol. 19, pp. 321–326, 1991.

[4] P.J.Basser and C.Pierpaoli, "Microstructual and physiological features of tissues elucidated by quantitative diffusion tensor mri," *Magn. Reson. Med.*, vol. 111(B), pp. 209–219, 1996.

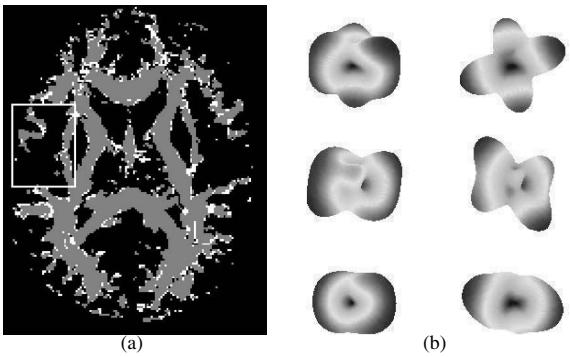

(a) (b)

Figure 4: (a) Classification: white, gray, and black voxels are identified as two-fiber, one-fiber, and isotropic diffusion respectively, (b) Shapes of $d(\mathbf{x}, \theta, \phi)$ at three particular voxels are shown in upper, middle and lower rows. The $A_{l,m}(\mathbf{x})$'s used in (2.2) to obtain d on the left and right columns correspond to those obtained using the least-squares and our model respectively.

[5] DS Tuch, RM Weisskoff, JW Belliveau, and VJ Wedeen, "High angular resolution diffusion imaging of the human brain," in *Proc. of the 7th ISMRM*, Philadelphia, 1999, p. 321.

[6] VJ Wedeen, TG Reese, DS Tuchand MR Weigel, J-G Dou, and RM Weisskoffand D. Chesler, "Mapping fiber orientation spectra in cerebral white matter with fourier transform diffusion mri.," in *Proc. of the 8th ISMRM*, Denver, 2000, p. 82.

[7] E. O. Stejskal and J. E. Tanner, "Spin diffusion measurements: Spin echoes in the presence of a time-dependent field gradient," *Chem. Phys.*, vol. 42, pp. 288C292, 1965.

[8] P.J.Basser J. Mattiello and D. Lebihan, "Estimation of the effective self-diffusion tensor from the nmr," *Spin Echo. J. Magn. Reson.*, vol. series B 103, pp. 247–254, 1994.

[9] PJ Basser, J Mattiello, and D LeBihan, "Mr diffusion tensor spectroscopy and imaging," *Biophys*, vol. 66:259, pp. 267, 1994.

[10] TL Chenevert, JA Brunberg, and JG Pipe, "Anisotropic diffusion in human white matter: demonstration with mr techniques in vivo," *Radiology*, vol. 177, pp. 401–405, 1990.

[11] EW Hsu and S. Mori, "Analytical expression for the nmr apparent diffusion coefficients in an anisotropy system and a simplified method for determing fiber orientation," *Magn Reson Med*, vol. 34, pp. 194–200, 1995.

[12] B. C. Vemuri, Y. Chen, and M. Rao et. al., "Fiber tract mapping from diffusion tensor mri," in *Proc. of 1st IEEE Workshop on Variational and Level Set Methods in Computer Vision*, Vancouver, B.C. Canada, 2001, pp. 81–88.

[13] T. Mcgraw, B.C Vemuri, and Y. Chen et. al., "Dt-mri denoising and neuronal fiber tracking," *MedIA*, vol. 8, pp. 95–111, 2004.

[14] A.L.Alexander, K.M.Hasan, M.Lazar, J.S.Tsuruda, and D.L.Parker, "Analysis of partial volume effects in diffusion-tensor mri," *Magn Reson Med*, vol. 45, pp. 770–780, 2001.

[15] LR Frank, "Characterization of anisotropy in high angular resolution diffusion weighted mri," in *Proc. of 9th ISMRM*, Glasgow,Scotland, 2001, p. 1531.

[16] LR Frank, "Anisotropy in high angular resolution diffusion-weighted mri," *Magn Reson Med*, vol. 45, pp. 935–939, 2001.

[17] D.C.Alexander, G.J.Barker, and S.R.Arridge, "Detection and modeling of non-gaussian apparent diffusion coefficient profiles in human brain data," *Magn.Reson.Med.*, vol. 48, pp. 331–340, 2002.

[18] Z. Wang, B.C. Vemuri, Y. Chen, and T. Mareci, "A constrained variational principle for direct estimation and smoothing of the tensor field from complex dwi," in *IEEE TMI*, to appear.

[19] L. Rudin, S. OSher, and E. Fatemi, "Nonlinear total variation based noise removal algorithm," *Physica D*, vol. 60, pp. 259–268, 1992.

[20] P.Blomgren and T.Chan, "Color tv: total variation methods for restoration of vector-valued images," *IEEE Trans. on Image Processing*, vol. 7(3), pp. 304–309, 1998.

[21] A.Chambolle and P-L.Lions, "Image recovery via total variation minimization and related problems," *Numerische Mathematik*, vol. 1(76), pp. 167–188, 1997.